The Astrophysical Journal, 627:986–1000, 2005 July 10

A DYNAMICAL SIMULATION OF THE DEBRIS DISK AROUND HD 141569A

D. R. Ardila,[1] S. H. Lubow,[2] D. A. Golimowski,[1] J. E. Krist,[2] M. Clampin,[3] H. C. Ford,[1] G. F. Hartig,[2] G. D. Illingworth,[4] F. Bartko,[5] N. Benítez,[1] J. P. Blakeslee,[1] R. J. Bouwens,[1] L. D. Bradley,[1] T. J. Broadhurst,[6] R. A. Brown,[2] C. J. Burrows,[2] E. S. Cheng,[7] N. J. G. Cross,[1] P. D. Feldman,[1] M. Franx,[8] T. Goto,[1] C. Gronwall,[9] B. Holden,[4] N. Homeier,[1] L. Infante,[10] R. A. Kimble,[3] M. P. Lesser,[11] A. R. Martel,[1] F. Menanteau,[1] G. R. Meurer,[1] G. K. Miley,[8] M. Postman,[2] M. Sirianni,[2] W. B. Sparks,[2] H. D. Tran,[12] Z. I. Tsvetanov,[1] R. L. White,[2] W. Zheng,[1] and A. W. Zirm[8]

Received 2004 July 16; accepted 2005 March 20

ABSTRACT

We study the dynamical origin of the structures observed in the scattered-light images of the resolved debris disk around HD 141569A. The disk has two conspicuous spiral rings and two large-scale spiral arms. We explore the roles of radiation pressure from the central star, gas drag from the gas disk, and the tidal forces from two nearby stars in creating and maintaining these structures. The disk's color, scattering function, and infrared emission suggest that submicron-sized grains dominate the dust population observed in scattered light. CO observations indicate the presence of up to 60 $M_\oplus$ of gas. The dust grains are subject to the competing effects of expulsive radiation pressure ($\beta > 1$, where β is the ratio of the radiation and gravitational forces) and retentive gas drag. We use a simple one-dimensional axisymmetric model to show that the presence of the gas helps confine the dust and that a broad ring of dust is produced if a central hole exists in the disk. This model also suggests that the disk is in a transient, excited dynamical state, as the observed dust creation rate applied over the age of the star is inconsistent with submillimeter mass measurements. We model in two dimensions the effects of a flyby encounter between the disk and a binary star in a prograde, parabolic, coplanar orbit. We track the spatial distribution of the disk's gas, planetesimals, and dust. We conclude that the surface density distribution reflects the planetesimal distribution for a wide range of parameters. Our most viable model features a disk with initial radius 400 AU, a gas mass of 50 $M_\oplus$, and $\beta = 4$ and suggests that the system is being observed within 4000 yr of the flyby periastron. The model reproduces some features of HD 141569A's disk, such as a broad single ring and large spiral arms, but it does not reproduce the observed multiple spiral rings or disk asymmetries nor the observed clearing in the inner disk. For the latter, we consider the effect of a $5M_J$ planet in an eccentric orbit on the planetesimal distribution of HD 141569A.

Subject headings: circumstellar matter — hydrodynamics — planetary systems: formation — planetary systems: protoplanetary disks — stars: individual (HD 141569)

1. INTRODUCTION

Debris disks around main-sequence stars are dusty, optically thin, and gas-poor. Radiation pressure (RP) and Poynting-Robertson (PR) drag eliminate dust grains on timescales shorter than the stellar age, so the observed dust must be continuously replenished by collisions among, or evaporation of, planetesimals (Backman & Paresce 1993). The *Infrared Astronomical Satellite* (*IRAS*) and the *Infrared Space Observatory* (*ISO*) revealed over 100 stars with far-infrared excesses indicating the presence of debris disks. However, spatially resolved images of these disks are relatively rare: only about a dozen debris disks have been resolved since the early 1980s (see Zuckerman [2001] and references therein).

The resolved disks are not featureless. They frequently display warps, spiral structures, and other azimuthal and radial asymmetries. Different mechanisms have been suggested to explain these features. They may be caused by interactions between the dust and the gas in the disk (Takeuchi & Artymowicz 2001, hereafter TA01), the formation of small planets (Kenyon & Bromley 2004), the dynamical forces of embedded planets (Ozernoy et al. 2000), or stellar-mass companions (Larwood & Kalas 2001; Augereau & Papaloizou 2004; Quillen et al. 2005). Whatever their cause(s), the features observed in the dust disks provide insight into the characteristics of the unseen planetesimal population and illuminate the dynamical processes of young planetary systems.

HD 141569A (A0 V; age 5 ± 3 Myr; Weinberger et al. 2000) has a resolved circumstellar debris disk. Its *Hipparcos* distance is 99 pc from the Sun, and it has comoving M2 V and M4 V companions separated by 1.″4 and located at distances of 7.″55 and 8.″93, respectively (Weinberger et al. 2000; Augereau et al. 1999). The disk was first resolved in scattered light by Weinberger et al. (1999) and Augereau et al. (1999), using the *Hubble Space Telescope* (*HST*) Near-Infrared Camera Multi-Object Spectrometer (NICMOS). Mouillet et al. (2001) imaged the disk

[1] Department of Physics and Astronomy, Johns Hopkins University, 3400 North Charles Street, Baltimore, MD 21218.
[2] Space Telescope Science Institute, 3700 San Martin Drive, Baltimore, MD 21218.
[3] NASA Goddard Space Flight Center, Code 681, Greenbelt, MD 20771.
[4] UCO/Lick Observatory, University of California, Santa Cruz, CA 95064.
[5] Bartko Science and Technology, 14520 Akron Street, Brighton, CO 80602.
[6] Racah Institute of Physics, Hebrew University, Jerusalem 91904, Israel.
[7] Conceptual Analytics, LLC, 8209 Woburn Abbey Road, Glenn Dale, MD 20769.
[8] Leiden Observatory, Postbus 9513, 2300 RA Leiden, Netherlands.
[9] Department of Astronomy and Astrophysics, Pennsylvania State University, 525 Davey Lab, University Park, PA 16802.
[10] Departmento de Astronomía y Astrofísica, Pontificia Universidad Católica de Chile, Casilla 306, Santiago 22, Chile.
[11] Steward Observatory, University of Arizona, Tucson, AZ 85721.
[12] W. M. Keck Observatory, 65-1120 Mamalahoa Highway, Kamuela, HI 96743.

with the *HST* Space Telescope Imaging Spectrograph (STIS) and noted strong brightness asymmetries. These observations have recently been complemented by images from *HST*'s Advanced Camera for Surveys (ACS) (Clampin et al. 2003, hereafter C03). Together, these scattered-light images reveal very complex structure, including an inner clearing within 175 AU of the star, a bright spiral ring with a sharp inner edge from 175 to 215 AU, a faint zone from 215 to 300 AU, and a broad spiral ring from 300 to 400 AU (C03). These distances are measured along the projected disk's southern semimajor axis. (For convenience, we hereafter refer to the two tightly wound spiral rings simply as "rings.") C03 also observed two low-intensity, large-scale spiral arms in the outermost part of the disk, which they attributed to tidal interaction with the M dwarf companions.

The influence of the M dwarf companions on the disk's morphology was first discussed by Weinberger et al. (2000). They argued that if all three stars were coplanar with the disk, the system would not be stable. Given its young age, however, the system may be bound. With this assumption, Weinberger et al. (2000) concluded that resonant interactions between the companions and the disk do not account for the disk structure. Assuming that the companions revolve around the primary star in a highly eccentric orbit, Augereau & Papaloizou (2004) constructed dynamical models of the optical disk comprising dust grains that respond to the stellar gravitational field. They assumed that the grains are large enough that RP, PR drag, and gas drag are unimportant. They also ignored the presence of the large-scale spiral arms reported by C03. Their model reproduces the general appearance of the brightness asymmetries observed in the disk. Quillen et al. (2005) constructed hydrodynamic models of HD 141569A's gas disk without dust and also concluded that the companions lie in an eccentric orbit. Their models reproduced the large-scale spiral arms (even after several periastron passages) and some other disk asymmetries.

TA01 modeled the interaction between disks of gas and intermediate-size ($\gtrsim 8$ μm) dust grains, and Lecavelier Des Etangs et al. (1998) considered disks with very small particles. It is not clear whether the conditions explored by any of these models are the correct ones for the scattered-light images of the disk around HD 141569A. In § 2, we argue that submicron-sized grains account for most of the scattering opacity at optical wavelengths. Such small grains are subject to RP, which quickly expels them from the disk. The gas detected in the disk (Zuckerman et al. 1995) tempers somewhat the short blowout timescales, but its mass is not enough to dominate the dynamics of the dust (§ 3). In this paper, we explore the effects of strong RP, gas drag, and gravity on small dust grains, using HD 141569A's disk as a benchmark. We simultaneously track the behavior of three different populations: the unseen planetesimals controlled by gravity, the gas controlled by gravity and volumetric fluid forces, and the dust controlled by gravity, RP, and gas drag. The insights obtained from this analysis should be applicable to other systems in which RP is important.

In § 2, we review the observational constraints that every model of the system should satisfy. We consider evidence that indicates the dominance of submicron-sized grains, and we set limits on the amount of gas in the disk. In § 3, we explore the interaction between gas and dust by means of a one-dimensional model. We show that the gas slows the outward motion of the dust and can produce broad ringlike structures. In § 4, we present two-dimensional dynamical simulations of the interactions between planetesimals, dust grains, gas, and the three stars. Assuming that the two M dwarf companions are comoving but unbound, we find that a recent parabolic flyby causes some of the observed disk structure, including the large-scale arms. However, our models produce a more disorganized disk than is observed. We argue that the central hole in the disk can be produced by a planet with a mass a few times that of Jupiter (or, alternatively, some number of smaller planets) in a highly eccentric orbit about the primary star.

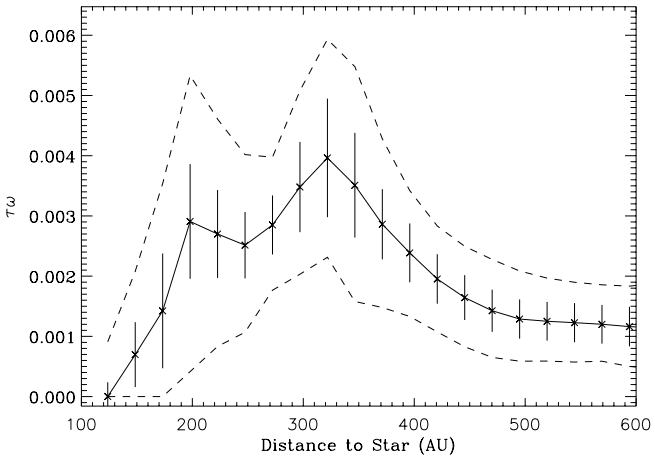

FIG. 1.—Optical depth profile (proportional to the surface density) of the disk shown in Fig. 5 of C03, derived from the median values of concentric annuli centered on the estimated geometric center of the spiral rings. The error bars indicate the standard deviation, and the dashed lines indicate the upper and lower values in each annulus.

2. OBSERVATIONAL CONSTRAINTS

2.1. *Grain Size*

Figure 1 shows the optical depth profile of the disk, taken from Figure 5 of C03. This profile represents the median values of concentric annuli centered on the primary star. Drawn from a composite of F435W (ACS *B*-band) and F606W (ACS broad *V*-band) images, it is roughly indicative of the optical characteristics of the disk at 0.5 μm. Power-law fits to the inner and outer edges of the profile (using as errors the standard deviation at every radius) give $r^{5\pm3}$ for $r < 200$ AU and $r^{-2.8\pm0.6}$ for 320 AU $< r <$ 500 AU. Beyond 500 AU, the average azimuthal brightness seems to be dominated by the light from HD 141569BC. The optical depth profile indicates that the amount of mass in $\sim$0.5 μm sized grains is $\sim$0.01 $M_\oplus$ (assuming a constant dust opacity of 2×10^4 cm^2 g^{-1} and an albedo of $\sim$0.5; see Wood et al. 2001).

The disk is occulted by ACS's coronagraphic mask within $\sim$150 AU. Fisher et al. (2000) and Marsh et al. (2002) detected mid-infrared thermal emission within this radius, and Marsh et al. (2002) concluded that the optical depth at 1.1 μm decreases by a factor of $\sim$4 within this region. Li & Lunine (2003, hereafter LL03) modeled the thermal spectrum of the disk by assuming a density profile similar to the one shown in Figure 1. Their model suggests that the reduced emission within $\sim$150 AU is due to reduced dust density and not to a change in the scattering properties of the grains.

C03 reported that the disk is redder than the star, with color excesses of $\Delta(B - V) = 0.21$ and $\Delta(V - I) = 0.25$. They also reported no color variation as a function of distance from the star (which supports our use of a constant opacity in the mass calculation above). C03 inferred that the disk's colors are consistent with astronomical silicate grains having a size distribution

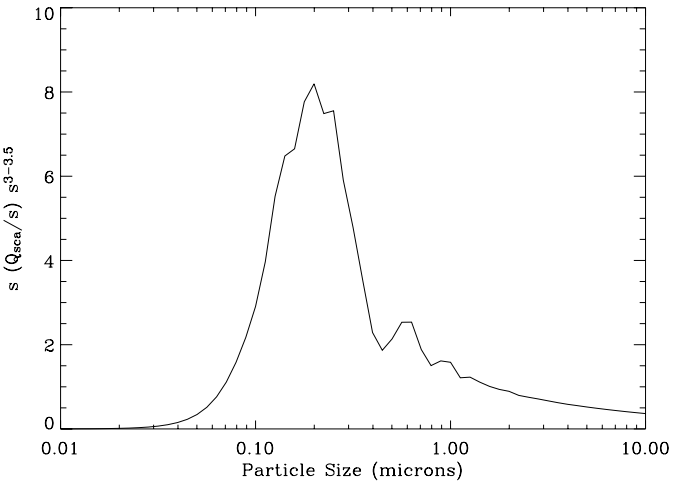

FIG. 2.—Scattering opacity at 0.5 μm as a function of grain size. The scattering opacity is proportional to the mass opacity (the scattering cross section, $\sigma_{sca} = Q_{sca}\pi s^2$, divided by the particle mass, $\propto s^3$) weighted by the number of particles ($\propto s^{-3.5}$) and the particle mass ($\propto s^3$), where s is the particle size. The scattering efficiency Q_{sca} is that of a compact astronomical silicate (Laor & Draine 1993; Draine & Lee 1984). To conserve the area under the curve with a logarithmic abscissa, the ordinate has been multiplied by s.

of $s^{-3.5}$ and a minimum radius of $s \sim 0.4$ μm. Augereau & Papaloizou (2004) used the same color information to derive lower size limits between $\sim$0.1 and 3.1 μm. The existence of such small grains is also implied by the small scattering asymmetry factor ($0.15 < g < 0.25$)[13] of the Henyey-Greenstein function derived by C03. The multicomponent models by LL03 suggest that the minimum grain size is between 0.1 and 10 μm: the smaller limit produces too little emission in the *IRAS* 60 μm band, and the larger limit produces too much emission in the *IRAS* 60 and 100 μm bands. Taken together, these arguments imply that there is a population of grains whose radii may extend down to 0.1 μm.

The combined influences of the reduced scattering efficiency (Q_{sca}) of small grains and the small number of large grains (assuming a size distribution going as $s^{-3.5}$) produce sharply peaked scattering opacity, which indicates that the grain sizes responsible for the optical images of the disk are on the order of the wavelength of observation. Figure 2 shows the scattering opacity at 0.5 μm as a function of grain radius for astronomical silicate grains (Laor & Draine 1993; Draine & Lee 1984) larger than 0.01 μm. The scattering opacity is expressed as the scattering cross section per unit mass ($\propto \sigma_{sca} s^{-3}$, where $\sigma_{sca} = Q_{sca}\pi s^2$), weighted by the mass and the number of grains at each radius s (Miyake & Nakagawa 1993). The function is centered at 0.2 μm, with a characteristic width of $\Delta s \sim 0.3$ μm. The sharp decrease in the scattering opacity of grains larger than 0.2 μm is determined by the behavior of the first scattering peak in Q_{sca}. In the limit of large grains, the scattering opacity decreases more slowly ($\sim s^{-0.5}$, for intervals of constant ds/s). For this dust model, 1 μm grains scatter $\sim$8 times less than 0.2 μm grains and $\sim$3 times more than 10 μm grains. The location and width of the peak in the scattering opacity depend on the surface properties of the grains and the exact mixture of silicates, ices, and empty space. For example, increasing porosity moves the peak to smaller sizes, and less reflecting grains broaden the peak and move it to larger sizes (Bohren & Huffman 1983).

[13] Because of a typo, the value of g for the HD 141569A disk is quoted as $g = 0.25-0.35$ in C03.

If, as suggested by the disk colors, the phase of the scattering function and the spectral energy distribution, submicron-sized grains exist in the disk, their dynamics are strongly influenced by RP. According to TA01, the ratio (β) of the forces from RP and gravity is $\sim$4 for a 1 μm dust grain, and $\beta \sim 20$ for $s \sim 0.05$ μm. For the very porous grains assumed by LL03, $\beta \sim 12$ for $s \sim 1$ μm. Formally, and in the absence of gas, grains with $\beta > 0.5$ ("β meteoroids") are expelled from the disk. Grains with large β acquire a radial velocity on the order of their Keplerian velocity in $T_{esc} \sim (P/2\pi)/\beta$, where P is the orbital period at a given position (TA01). At the edge of a 500 AU disk around a 2.3 $M_\odot$ star, $T_{esc} \sim 300$ yr for $\beta = 4$. Such short expulsion timescales are somewhat mitigated by the effects of another force: the gas drag.

2.2. *Gas Content*

Zuckerman et al. (1995) measured the gas content of HD 141569A's disk using the detected $J = 2 \rightarrow 1$ transition for ^{12}CO and the upper limit on the same line for ^{13}CO. They assumed that the star's distance was 200 pc, that its disk had a radius of 130 AU, and that $H_2/CO \sim 10{,}000$. They calculated gas masses between 20 and 460 $M_\oplus$ for optically thin and optically thick limits, respectively. Assuming that the gas and dust disks are coincident, we recompute the gas content using the observed extent of the optical disk and the measured *Hipparcos* distance to HD 141569A of 99 pc.

Zuckerman et al. (1995) have generously provided us with their unpublished digitized CO spectra, which are reproduced in Figure 3. The spectra show a double peak characteristic of sharp disks, although the depths of the central line emission in both measurements are a little over 1 σ per resolution element. Assuming an disk inclination of 55° (C03), the velocity difference between the peaks is 3.8 ± 1.0 km s^{-1}, which implies emission at 380^{+120}_{-180} AU. (The upper limit is dictated by the size of the optical disk.) Assuming $H_2/CO \sim 4000$ (Lacy et al. 1994), the optical depth of the central line is $\tau = 1.5 \times 10^6 [\Sigma/(1\ \mathrm{g\ cm^{-2}})](5.5\ \mathrm{K}/T)^{5/2}$, where Σ is the surface density and T is the excitation temperature of the gas (Beckwith & Sargent 1993). Nondetection of the ^{13}CO line yields an upper limit of $T = 30$ mK, so the opacity of the ^{12}CO line is uncertain. If the ^{12}CO line is optically thick, then we

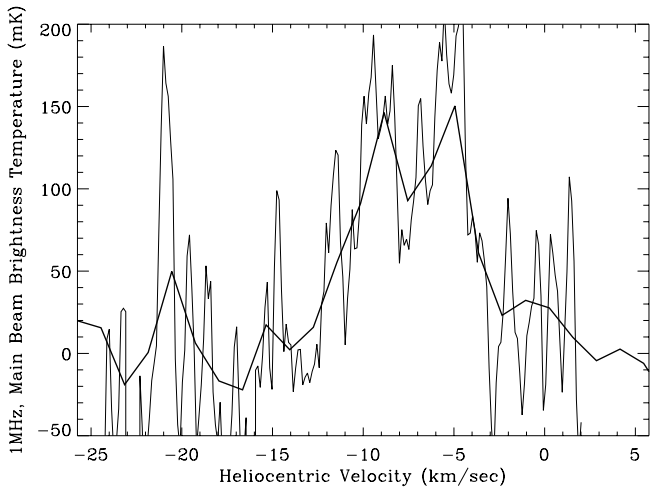

FIG. 3.—Spectra of ^{12}CO $J = 2 \rightarrow 1$ transition with resolutions of 1 MHz (*thick curve*) and 100 KHz (*thin curve, after three-point smoothing*) from Zuckerman et al. (1995). Although the depth of the central depression is $\sim$1 σ, it is present in both spectra.

obtain a gas mass of $\lesssim 60\ M_\oplus$. If the line is optically thin and fills a disk of radius 380 AU, we obtain a gas mass of $0.02\ M_\oplus$. In each case, the gas is assumed to be in local thermal equilibrium (LTE).

3. THE DYNAMICS OF HIGH-β PARTICLES

We now explore the interaction between small dust grains, gas, and the radiation and gravitational fields of HD 141569A, while ignoring the presence of the binary companions. Most of the results of this axisymmetric treatment should be applicable to other debris and gas disks in which RP is important. The regime that we explore here is that of modest amounts of gas (up to 50 $M_\oplus$) and not very large values of β ($\beta \sim 4-10$). Our calculations are complementary to those of Lecavelier Des Etangs et al. (1998), who consider $\beta \gtrsim 100$, and TA01, who consider $\beta \lesssim 1$. Note that Lecavelier Des Etangs et al. (1996) have shown that if the observed dust particles all have $\beta < 0.5$, a single ring of planetesimals in a gasless disk will produce a dust disk with surface density given by r^{-3}, as observed here.

We solve the equations of motion for a dust grain, assuming that it is subject to RP, PR drag, and gas drag. The gas is assumed to be in a circular orbit, and we assume the same dust model as TA01. The force of the gas on the dust is given by

$$\boldsymbol{F_g} = -\pi \rho_g s^2 \left(v_T^2 + \Delta v^2\right)^{1/2} \Delta \boldsymbol{v}, \tag{1}$$

where ρ_g is the gas density, s is a dust grain radius, v_T is 4/3 times the thermal velocity of the gas, and $\Delta \boldsymbol{v}$ is the relative velocity of the dust with respect to the gas. To determine the trajectory of a dust grain, we assume that the surface density of the gas (as well as that of planetesimals) decreases radially as $r^{-1.5}$. This function is characteristic of the dust surface density of optically thick protoplanetary disks (Osterloh & Beckwith 1995). In other words, we assume that the gas and planetesimal density profiles of the optically thin disks are the same as the dust density profile of the optically thick disks. We further assume (unless otherwise stated) that the gas is in LTE, with temperature

$$T_g = 278 \left(\frac{L_*}{L_\odot}\right)^{1/4} r_{\rm AU}^{-1/2}\ {\rm K}, \tag{2}$$

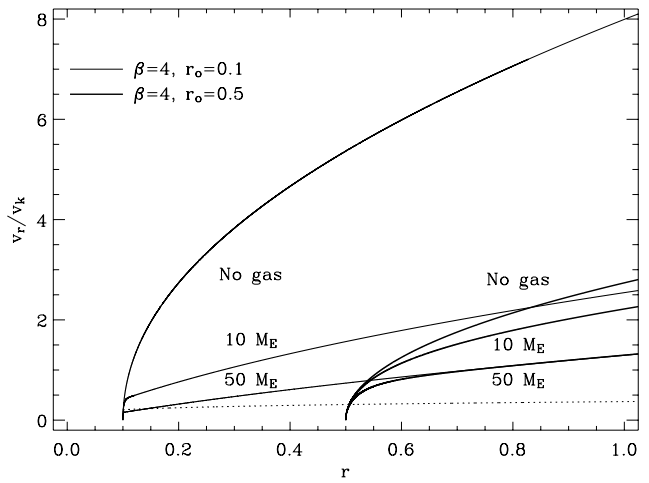

FIG. 4.—Radial velocity (divided by the local Keplerian velocity) as a function of radii, for $\beta = 4$ dust particles launched from two different points: $r_o = 0.1$ (*thin lines*) and 0.5 (*thick lines*). The behavior of the dust particles with different amounts of gas is shown: no gas (*top curve*), 10 $M_\oplus$ of gas, and 50 $M_\oplus$ of gas (*bottom curve*). The dotted line is the thermal sound speed of the gas.

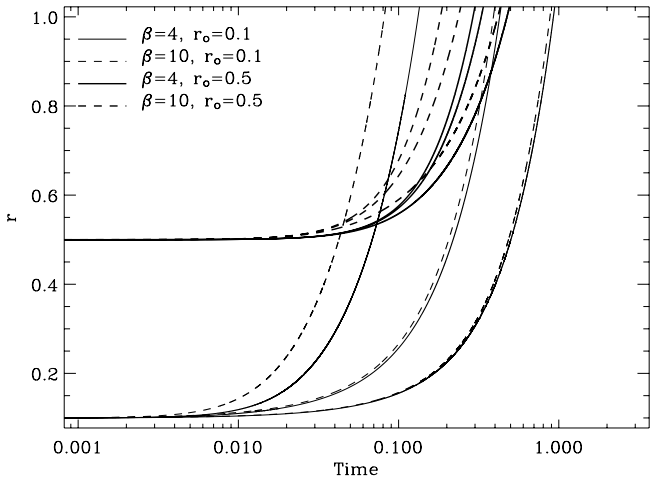

FIG. 5.—Position as a function of time for dust particles released at two different positions: 0.1 (*thin lines*) and 0.5 units (*thick lines*), for a unit disk of gas in thermal equilibrium around a 2.3 $M_\odot$ star. The unit of time is such that the orbital period at the outer edge of the disk is 2π. (If the disk is 1000 AU in radius, 1 time unit is 3325 yr.) The solid lines trace particles with $\beta = 4$, while the dashed lines trace particles with $\beta = 10$. For each set, three lines are shown. From the left, these represent no gas, 10 $M_\oplus$ of gas, and 50 $M_\oplus$ of gas. Note that for large amounts of gas, there is little difference between particles with $\beta = 10$ (*dashed lines*) and $\beta = 4$ (*solid lines*).

where $L_* = 22.4\ L_\odot$ is the stellar luminosity (Backman & Paresce 1993). This implies that H, the vertical scale of the gas disk, is given by

$$\frac{H}{r} = 0.185 \left(\frac{L_*}{L_\odot}\right)^{1/8} \left(\frac{r}{1000\ {\rm AU}}\right)^{1/4}. \tag{3}$$

Without gas, the radial velocity of a dust grain is given by

$$v_r(r_o, r) = \sqrt{2} v_o \left[\beta - \frac{1}{2} - \frac{r_o^2}{2r^2} + \frac{r_o}{r}(1-\beta)\right]^{1/2}, \tag{4}$$

where r_o is the radius at which the dust grain is created and v_o is the Keplerian velocity at r_o. In general, there is not an analytic expression for the radial velocity of a dust grain in the presence of gas. For the range of parameters we are considering here, the dust grain speeds are supersonic and almost radial at the outer edge of the disk (Fig. 4). The dimensionless stopping time (the stopping time in units of the inverse local Keplerian frequency) at the edge of the disk is given by (TA01):

$$T_s \sim \frac{4\rho_d s v_{\rm K}}{3\rho_g r v_r} \sim 86.6 \frac{1}{\beta} \frac{M_\oplus}{M_g} \frac{1}{v_r/v_k}, \tag{5}$$

which, for the parameters considered here, is $\lesssim 1$. Note that, unlike in the case considered by Lecavelier Des Etangs et al. (1998), the radial velocity shown here does not have a deceleration region, because in our case the gas surface density decreases with radius: the radiation pressure always dominates the dynamics of the dust.

The effect of gas on the grains depends on where the grains were created. Figure 5 shows that for a fixed value of β and without gas, particles that start closer to the star soon overtake particles farther out. This changes with the presence of gas, because the drag force decreases outward, and for $\gtrsim 50\ M_\oplus$ of gas, the particles created closer in do not overtake those created farther out. Figure 5 also shows that the gas mass, not the grain size, determines the escape timescale: there is not much difference between

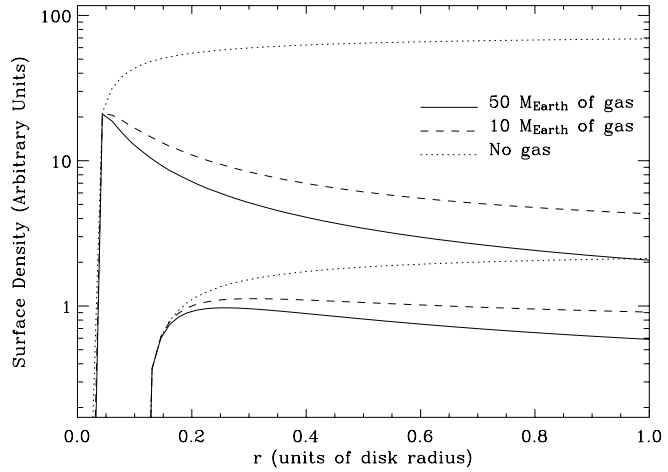

FIG. 6.—Steady state dust surface density as a function of distance for an isolated disk, with dust particles ($\beta = 4$; $s \sim 1$ μm according to TA01, or $s \sim 3$ μm for LL03) for the linear model (in which the rate of generation is proportional to the planetesimal surface density). Two sets of surface densities are shown: one for a disk in which the innermost dust generation radius is 0.1, and another for which it is 0.01. The dotted lines indicate the surface density with no gas, the dashed lines show the surface density with 10 $M_\oplus$ of gas, and the solid lines show the surface density with 50 $M_\oplus$ of gas. The gas is in LTE.

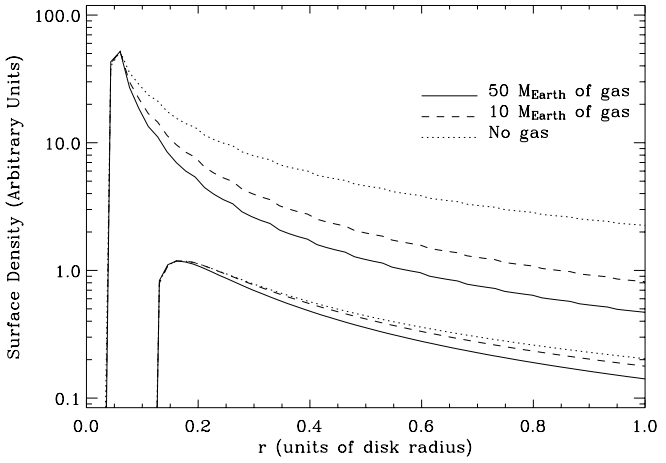

FIG. 7.—Steady state dust surface density as a function of distance for an isolated disk, but with the number of dust particles generated proportionally to the square of the planetesimal surface density. Lines are as in Fig. 6. Note that a broad ring is produced in all cases.

$\beta = 4$ and 10 for 50 $M_\oplus$ of gas, because both the gas drag and the RP are proportional to β.

If one assumes a rate of dust generation, the results of these calculations can be used to predict the steady state dust surface density in an isolated disk. In such a state, grains are continuously generated by collisions and then blown away by RP. The dust surface density (assuming conservation in the number of particles) is given by

$$\Sigma(r) \propto \int_{r_i}^{r} \frac{dN(r_o)}{v_r(r_o, r)r}, \qquad (6)$$

where r_i is the inner radius of dust generation, r_o is the position at which the grains are created, $dN(r_o)$ is the number of grains created at r_o, and $v_r(r_o, r)$ is the radial velocity at r of grains created at r_o. The dust creation rate per unit volume is taken to be $v_{\rm rel}\sigma_{\rm coll}N_p^2$, where N_p is the number of planetesimals per unit volume, $\sigma_{\rm coll}$ is the collision cross section, and $v_{\rm rel}$ is the relative velocity between the planetesimals, which is proportional to the dimensionless planetesimal disk thickness (H_p/r) times the Keplerian velocity (Thébault et al. 2003). This implies

$$dN(r_o) = v_{\rm rel}\sigma_{\rm coll}N_p^2 H_p 2\pi r_o\, dr_o \propto \Omega_k \Sigma_p^2 2\pi r_o\, dr_o, \qquad (7)$$

where Σ_p is the surface density of planetesimals at the creation point, which we assume to be proportional to $r^{-1.5}$.

In practice, this simple prescription (the "quadratic" dust generation prescription) may be affected by uncertainties in the planetesimal size distribution and in the relative velocities among the planetesimals. To explore the sensitivity of the results to the exact generation mechanism, we also consider a "linear" dust generation prescription in which $dN(r_o) \propto \Sigma_p r_o\, dr_o$.

For these calculations, we assume that the planetesimals and the gas are well mixed and therefore $H_p = H$. The resulting steady state surface densities are shown in Figures 6 and 7. In the figures, the unit length is 1000 AU. Figure 6 shows that even modest amounts of gas have a significant effect on the surface density profiles. The amounts of gas considered (10 and 50 $M_\oplus$) are not enough to confine the dust grains created at distances larger than 0.01, but gas drag sharpens the profiles, as it slows down the dust particles. Note that if dust creation starts very close to the central star, the resulting surface density profiles are effectively featureless. Figures 6 and 7 also show that a broad ring of dust is produced by truncating the dust creation within a certain radius. Just outside this limit, the number and surface density of planetesimals, and hence dust grains, are large. Far from the creation limit, the surface density of the dust decreases because of decreasing surface density of planetesimals and the geometric dilution of blown-out dust grains created at smaller radii. Thus, if a mechanism exists for preventing the creation of dust at small radii (for example, a planet that clears out the parent planetesimals), the result is, very naturally, a broad ring of dust at larger radii.

The rate at which dust is lost from the disk depends on the rate of planetesimal erosion. In principle, one can use the former to estimate the latter. LL03 calculated the amount of mass lost from HD 141569A's disk, assuming no gas, a grain size distribution $\propto s^{-3.3}$, $\beta = 1$ for grains of all sizes, and a constant rate of mass loss throughout the age of the system. They also assumed a surface density profile for the dust that is slightly different than the one shown in Figure 1. They concluded that 39 $M_\oplus$ of solid material has been lost, in particles with 1 μm $< s <$ 10 μm, from the disk due to RP and PR drag.

To examine the effect of the gas on the rate of mass loss, we consider a disk of radius 500 AU about HD 141569A without binary companions. Figure 8 shows the time required for small dust grains to move from a given radius to the edge of the disk for different values of gas mass and temperature. The presence of just 10 $M_\oplus$ of gas triples the escape time from 200 AU, and a colder disk confines the dust more than a hotter one. (Eq. [1] shows that, if we neglect v_T, a colder and thus denser gas disk produces more drag). Assuming a grain size distribution $\propto s^{-3.5}$, with 50 $M_\oplus$ of gas in LTE, varying escape times, the TA01 dust model, and a constant rate of mass loss, we determine that $\sim$700 $M_\oplus$ of solid material has been lost over the $\sim$5 Myr age of the disk, in particles with sizes 0.1 μm $< s <$ 8 μm. Without gas, $\sim$1200 $M_\oplus$ of solid material would have been lost. The difference with LL03 is due to the fact that in our calculation different size particles have different blowout timescales.

However, neither the estimate of LL03 nor ours can be correct. Because small grains ($\lesssim$10 μm) are quickly expelled from the disk, they must be the dominant component of the lost mass.

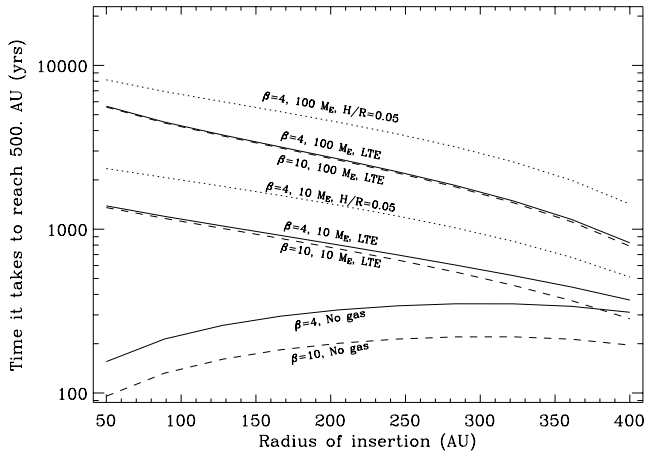

FIG. 8.—Time (in years) that it takes for a dust particle inserted with Keplerian velocity at different radii to reach 500 AU. The central star is 2.3 $M_\odot$. The gas sound speed is parameterized by the opening angle, H/r, where H is the disk thickness. Solid lines show $\beta = 4$, with gas in LTE; dashed lines show $\beta = 4$, with $H/r = 0.05$; dotted lines show $\beta = 10$, with gas in LTE. For each set of plots, from bottom to top, the lines represent models with no gas, 10 $M_\oplus$ of gas, and 100 $M_\oplus$ of gas (this is the gas amount within 500 AU).

If the grain size distribution is $\propto s^{-3.5}$ for grains with radii <1 mm, then grains up to 10 μm compose only 10% of the disk mass. The bulk of the dust mass is composed of large grains that are eliminated in much longer timescales. If the collisional processes responsible for the replenishment of small grains also produce large grains, then submillimeter observations should detect $\sim 10^4$ $M_\oplus$ of dust, which greatly exceeds the amount of ~ 2 $M_\oplus$ measured by Sylvester et al. (2001).

One possible solution to this discrepancy is that the dust is not generated with a power-law size distribution but with a distribution weighted toward small particles. The collisional evolution models of Thébault et al. (2003) suggest that, although large variations in the dust distribution are possible, most of the mass produced by the collisions is in large particles. These models assume that the collisional timescale is smaller than any other timescale in the disk.

Another possible solution is that the current rate of dust creation is larger than it has been in the past. This possibility is consistent with the idea that the disk has been recently stirred by a close encounter with a companion or unbound star. In § 4 we show that a parabolic encounter would occur over timescales on the order of 10^3 yr. Over this time the disk would lose (according to the model above) ~ 1 $M_\oplus$ of solids in small particles or ~ 10 $M_\oplus$ in particles up to 1 mm in size, close to the measured value. Observationally, the presence of ~ 0.01 $M_\oplus$ of solids in 0.5 μm sized particles (§ 2) suggests that there is currently on the order of 0.1 $M_\oplus$ in particles up to 8 μm in size, with the exact number depending on the assumed value of the opacity and dust size distribution.

Furthermore, these estimates support the idea of a single exciting event, like an encounter with an unbound companion, as opposed to repeated exciting events. In the models by Augereau & Papaloizou (2004), which assume a bound companion, repeated encounters are required to explain the brightness asymmetries in the debris disk.

4. A DYNAMICAL SIMULATION

The presence of large-scale spiral arms suggests that the dynamical influence of the binary companions, HD 141569B and C, is important. If they are coplanar with the disk, their center of mass is ~1250 AU away from the primary star and their separation is ~275 AU. Augereau & Papaloizou (2004) assumed that the companions are bound to HD 141569A in a very eccentric orbit. Their dynamical models show that close encounters between the companions and the disk produced well-developed spiral rings within the disk after only a few periastron passages. However, their models do not maintain large-scale spiral arms after a few orbits. Thus, within their model, the interaction geometry needed to create the spiral rings in the disk is not consistent with the presence of the large-scale spiral arms. The hydrodynamic model by Quillen et al. (2005) does produce spiral arms after repeated close encounters, because the viscosity and gas pressure help generate a spiral at every periastron passage. However, the amount of gas actually present in the disk (§ 2.2) discourages the notion that the dynamics of the dust conforms to that of the gas. Figure 5 shows that, for a reasonable range of gas masses, β-meteoroid grains responsible for the scattered-light disk are impeded by gas drag, but they are not bound by the gas. So the assumption by Quillen et al. (2005) that gas dynamics controls the observed structures in the dust disk is not appropriate.

4.1. *Assumptions and Methodology*

We assume that the encounter between the disk and the binary companions is a parabolic flyby, a situation known to produce spiral arms in dusty disks (Larwood & Kalas 2001). Such an encounter is consistent with the proper motion of the system. Within an error box of 0.″1, the position of the companions relative to HD 141569A has not changed over the 60 yr baseline of observations noted by Weinberger et al. (2000). The largest expected relative motion is obtained when the system is at periastron and the encounter occurs in the plane of the sky. In this scenario, the relative motion of the companions over 60 yr would be 0.″012, which is well inside the error box of the proper-motion measurements.

Dust grains are created by collisions of planetesimals. We assume that the planetesimals themselves experience gravity but not RP or gas drag. We also ignore self-gravity and the dynamical effects of the collisions. Our simulation is performed in two phases. First, we obtain the distribution of planetesimals and gas as a function of time. Then, for each planetesimal configuration, we generate a dust distribution and follow it as a function of time. We repeat this sequence for all planetesimal and gas configurations. At any given time, the dust in the disk consists of dust created at that time and dust remaining from earlier times.

The model is two-dimensional. We assign fixed masses of 2.3, 0.5, and 0.25 $M_\odot$ to HD 141569A, B, and C, respectively. We assume that the encounter is prograde, as a retrograde encounter fails to produce large-scale spiral arms. The phase of the encounter is fixed so that, at periastron, the three stars are aligned, with HD 141569B between A and C. (The results are mostly insensitive to the choice of phase.) Most of our simulations start with 10^4 planetesimals. The inner dust destruction limit is set at $r > 0.1$, where the distance r is measured relative to the separation of HD 141569A and HD 141569BC's barycenter at periastron. We assume that the initial surface density of planetesimals declines as $r^{-1.5}$. The outer radius of the planetesimal disk is a free parameter. Figure 9 shows the evolution of the planetesimals in a disk of unit radius. We define $T = 0$ as the time of periastron. The time unit is such that the period at unit distance is $2\pi[(m_1 + m_2)/m_1]^{1/2} = 7.2$ time units, where $m_1 = 2.3$ $M_\odot$ and $m_2 = 0.75$ $M_\odot$ (the latter is the sum of the companion masses). Note that the particular flyby configuration

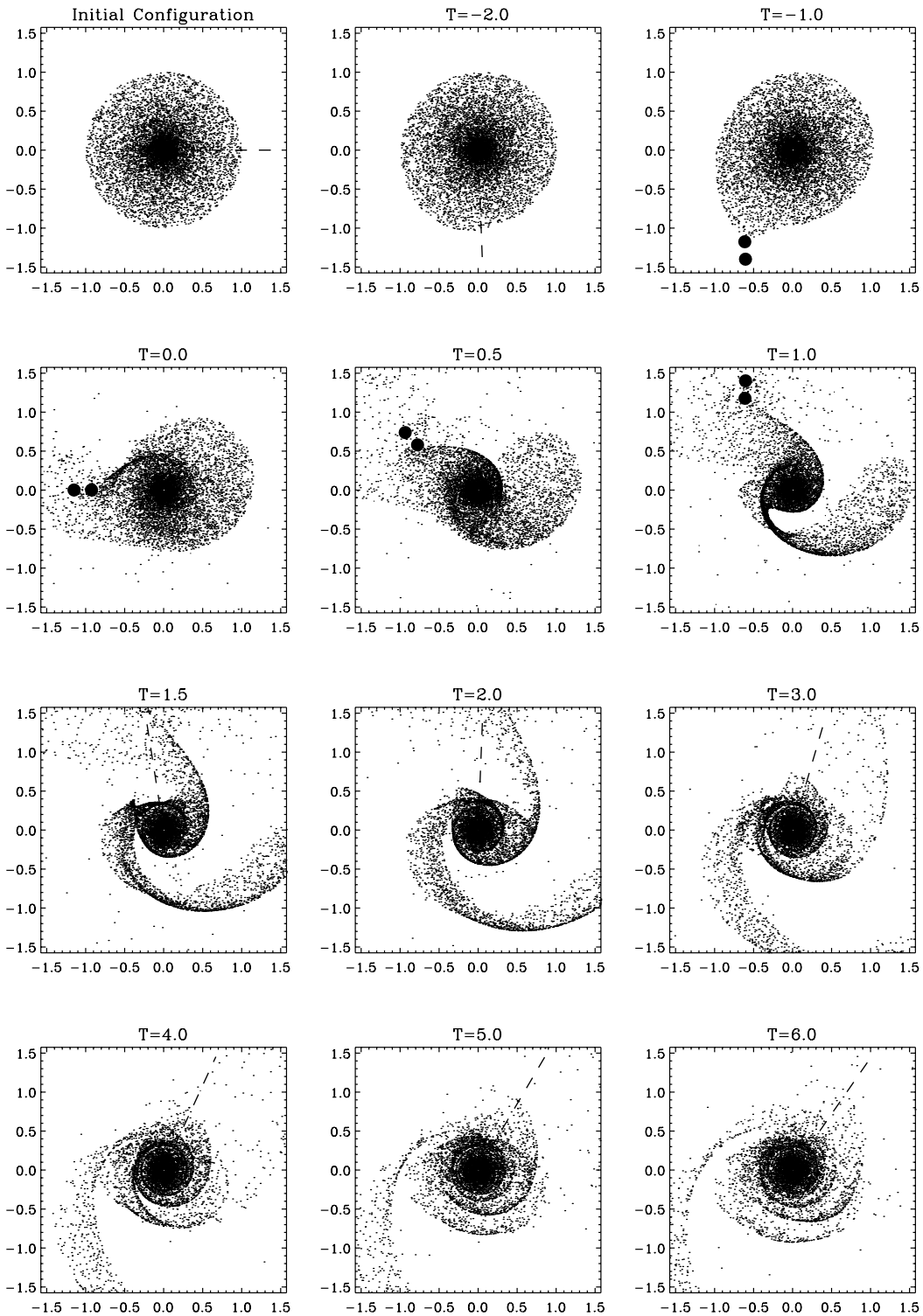

FIG. 9.—Planetesimal evolution as a function of time, for a prograde encounter. The periastron occurs at 1 unit distance, and in this particular example that is also the radius of the disk. The units of time are such that the period of a planetesimal at radius 1 is approximately 2π. The closest approach occurs at $T = 0.0$, with the largest of the companions closest to the center. The initial surface density distribution goes as $r^{-1.5}$. The position of the binary is indicated with two filled circles or a dashed line (when outside the presented frame).

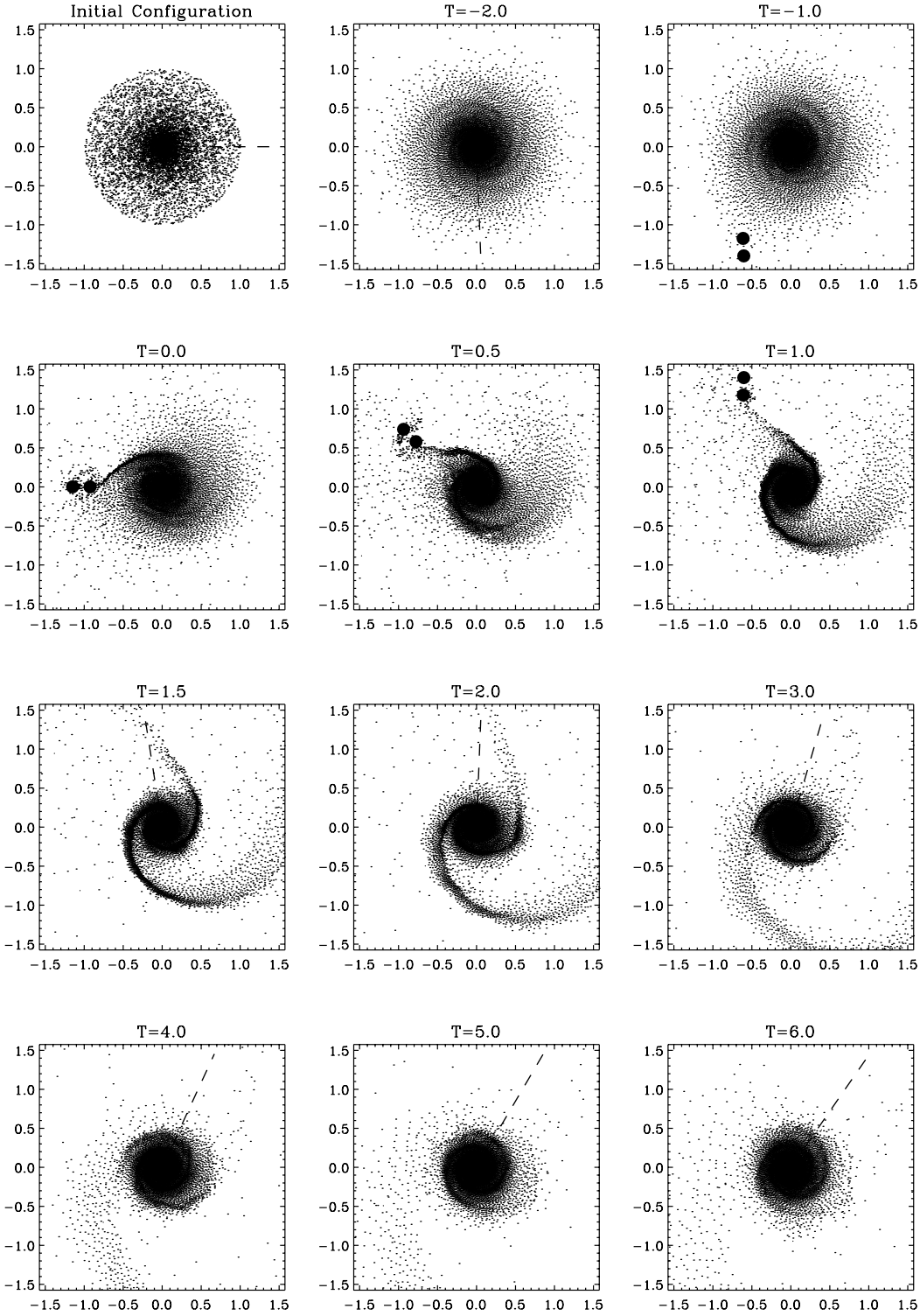

FIG. 10.—Gas evolution as a function of time. The gas has $H/r = 0.1$. The parameters of the simulation are the same as that of Fig. 9.

shown in Figure 9 shows that some planetesimals can be captured by the companions and therefore that some of the IR excess measured by *IRAS* may be associated with them.

The total mass of the gas is a free parameter. We consider gas disks with $r > 0.01$, an initial surface density profile $\propto r^{-1.5}$, and masses of 0, 10, 50, and 100 $M_{\oplus}$, before truncation by the encounter. We model the gas evolution using the smoothed particle hydrodynamics (SPH) formalism (Monaghan 1992), which allows one to track the motion of gas pseudoparticles using Lagrangian equations. Viscosity is parameterized according to equation (4.2) of Monaghan (1992). SPH permits the exploration of parameter space without a large investment of computer time but with limited resolution at small scales.

We explore different limits for the gas sound speed, which is parameterized by the disk opening angle, $H/r = c_s/r\Omega_K$, where H is the scale height of the gas, c_s is the speed of sound, and Ω_K is the Keplerian angular frequency at radius r. We consider gas with $H/r = 0.05$, 0.1, 0.2, and in LTE (eq. [3]). Brandeker et al. (2004) have shown that the empirical opening angle of the β Pictoris gas disk is $H/r \sim 0.28$, which is close to the expected

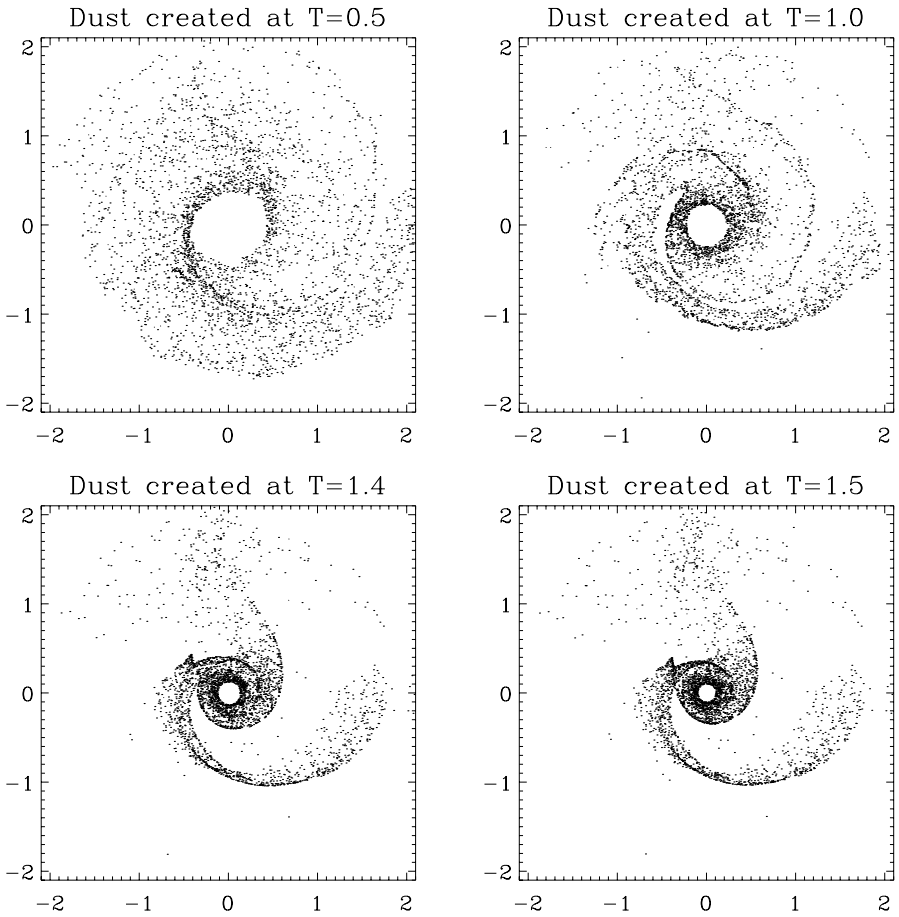

FIG. 11.—Observed profile at a given time, built by adding contributions from dust at previous times. In this example, $\beta = 4$ and $M_g = 50\ M_\oplus$, with $H/r = 0.1$, $T = 1.50$, and quadratic dust generation. The panels show the configuration of dust created at previous times and observed at $T = 1.50$. The plot shows the azimuthally averaged densities. These plots show that the disk is mainly cleared from the inside out.

LTE value at 1000 AU. Figure 10 shows the evolution of gas particles for the case of $H/r = 0.1$.

To simulate the dust grains, we consider the linear (particles created with $r > 0.1$) and quadratic (particles created with $r > 0.15$) dust creation prescriptions described in § 3. Particles are created every 0.01 time units. The ratio β, which couples the dust and the radiation, is also a free parameter. We explore two values: (1) $\beta = 4$, which corresponds to $s \sim 1$ μm (TA01) or $s \sim 4$ μm (LL03), and (2) $\beta = 10$, which corresponds to $s \sim 0.3$ μm (TA01) or $s \sim 1$ μm (LL03). We assume a single value of β per simulation, which is equivalent to assuming that the scattering opacity (Fig. 2) is a delta function.

To obtain the dust distribution at a given time, we consider all the dust particles created at previous times. Figure 11 shows the behavior of dust particles created at various time intervals for $\beta = 4$, $M_g = 50\ M_\oplus$, $H/r = 0.1$, and linear dust creation. The generations of particles were tracked to $T = 1.5$, and their respective surface densities were summed and azimuthally averaged at each time interval. This simulation tracks the entire history of dust generation, but in practice, dust blowout eliminates from the "current" surface density profile all the contributions of dust created before the last half time unit (i.e., $T - 0.5$).

4.2. *Simulation Results*

We now present our models for the flyby encounter with a composite disk of planetesimals, gas, and dust. Representative simulations are shown in Figures 12–16. Although most of the models are shown at $T = 1.5$, the images and profiles are representative of $0.8 \lesssim T \lesssim 2.0$. To give our spatial and temporal scales physical meaning, we set the distance between HD 141569A and the barycenter of the companions at $T = 1.5$, equal to that observed in the ACS images (C03). Thus, 1 distance unit corresponds to 718 AU, and 1 time unit corresponds to 1800 yr. The companions are out of the frames.

For each of Figures 12–16, we show the predicted logarithm of the density profile with linear dust generation (*top*) or quadratic dust generation (*bottom*). The use of the logarithmic stretch allows us to highlight faint features. The images are all normalized to the same arbitrary constant. In general, the color table of the bottom row has a lower limit value than the color table at the top row. This means that "white" in the bottom panels corresponds to somewhat less material than it does in the top panels. In this way, we can show faint features in the bottom row that would not be visible were we to use the same color table as that from the top row. This modification has little effect on the color the dark features, which implies that all panels within a given figure can be compared to each other. As mentioned before, an artificial inner hole has been set for the linear (at $r = 0.1$) and quadratic simulations (at $r = 0.15$). In each panel, the plot inset compares the measured density profile with the model density profile. The latter is normalized to the value measured at 500 AU.

Figure 12 shows the evolution of the dust structures for $\beta = 4$, $M_g = 50\ M_\oplus$, $H/r = 0.1$, an initial disk size of 1 unit distance, and both linear and quadratic dust generation. Figures 13

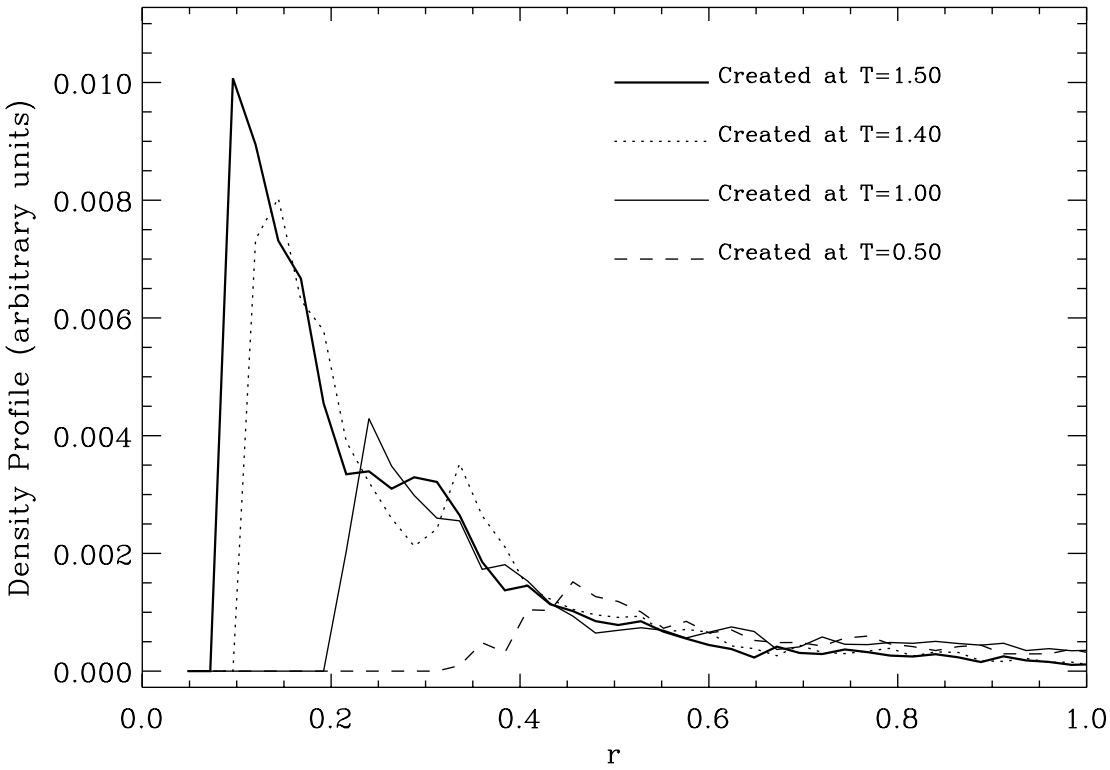

FIG. 11.—*Continued*

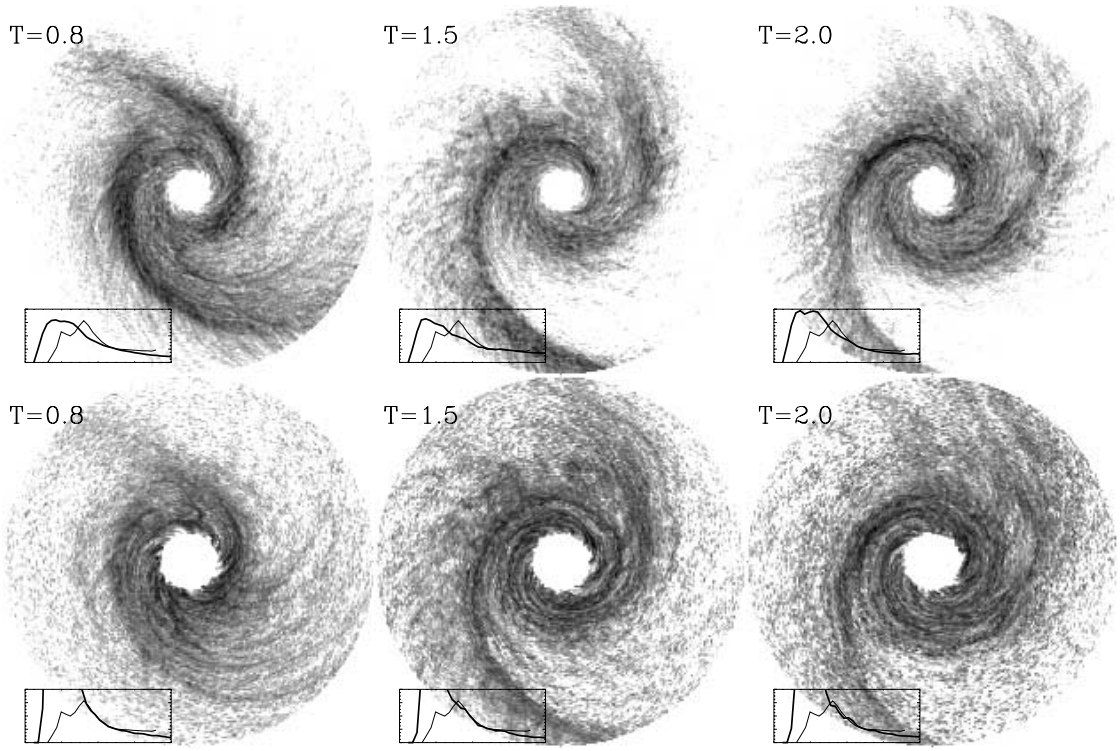

FIG. 12.—Time evolution of the dusty disk. The image shows the predicted density profile, azimuthally smoothed and Gaussian convolved to match the measurements. *Top*, Models with linear dust generation; *bottom*, models with quadratic dust generation. The profiles have been normalized to the same arbitrary maximum value. The panels display the logarithm of the density profiles. To highlight faint structure, the white color in the bottom panels corresponds to pixels 16 times fainter than those in the top panels. The companions are on top, just outside the frame. The plot insets compare the measured density profiles (*thin line*) with the model density profiles (*thick line*). To set the distance scale, the periastron is set at 718 AU. In these simulations, that is also the size of the initial disk. All models have $\beta = 4$, 50 $M_{\oplus}$ of gas, and $H/r = 0.1$. Three times are shown: $T = 0.8$, 1.5, and 2.0.

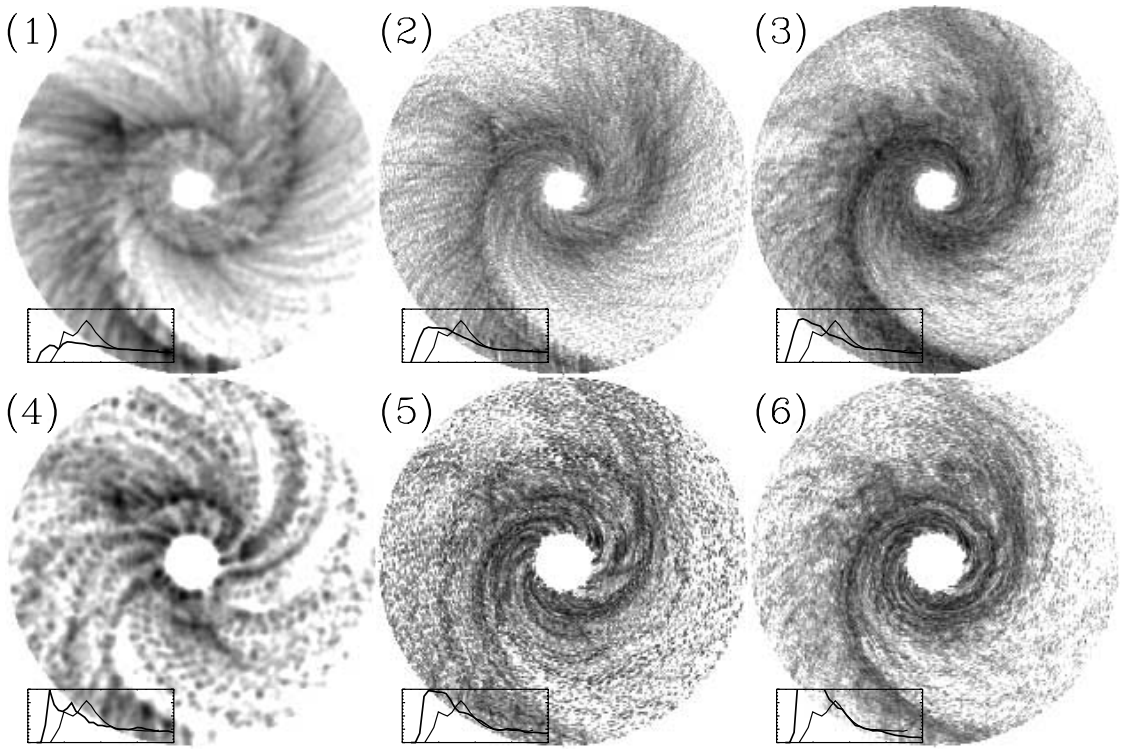

FIG. 13.—Effect of the amount of gas on the dust distribution. Profiles have been processed as in Fig. 12. Results of different model runs for $T = 1.5$. All models have $\beta = 4$. *Top*, Models with linear dust generation; *bottom*, models with quadratic dust generation. The white color in the bottom panels corresponds to pixels 4 times fainter than those in the top panels. *Top, left to right*: (1) No gas, linear dust generation; (2) 10 $M_\oplus$ of $H/r = 0.1$ gas, linear dust generation; (3) 50 $M_\oplus$ of $H/r = 0.1$ gas, linear dust generation. *Bottom, left to right*: (4) No gas, quadratic dust generation; (5) 10 $M_\oplus$ of $H/r = 0.1$ gas, quadratic dust generation; (6) 50 $M_\oplus$ of $H/r = 0.1$ gas, quadratic dust generation. In order to correct for artifacts of the dust generation process, the gasless models (panels 1 and 4) have been further processed by taking three-point medians in every pixel.

and 14 show the effect of the amount of gas on $\beta = 4$ and 10 dust particles, respectively. The sharp, concentric rings in the gasless models (panels 1 and 4) are artifacts of discrete dust generation. Figure 15 illustrates the role of the gas temperature, and Figure 16 shows the roles of disk sizes and planets. A side-by-side comparison of the observed disk and our favorite model is presented in Figure 17.

All the models look similar. Despite the dynamical importance of RP, the overall appearance of the dust disk resembles the underlying distribution of planetesimals. Figures 13 and 14 show that models with gas reproduce the observed profiles better than models without gas, but it is not clear that 10 $M_\oplus$ of $H/r = 0.1$ gas (panel 2 of each figure) is better than 50 $M_\oplus$ of $H/r = 0.1$ gas (panel 3 of each figure). There are no significant qualitative differences between the $\beta = 4$ and 10 conditions shown in Figures 13 and 14, respectively, as expected from the results in § 3. There is also no clearly preferred prescription for dust creation. The quadratic prescription does produce a more disorganized structure, as the dust is mostly generated in the denser spiral arms. Overdensities in the planetesimal distribution produce streams of matter in these models. Nevertheless, the combination of large β and quadratic dust generation with $H/r = 0.1$ gas (Fig. 14, panels 5 and 6) reproduces very well the decay of the surface density profile. Note that because more gas confines the dust better, the spirals in panels 3 and 6 of each figure look darker than the others.

Figure 15 shows that the simulations are sensitive to the gas temperature. Cold gas (panels 1 and 4) tends to produce sharper spiral structures than hot gas, because cold gas is denser and imparts greater drag on the dust. This effect is less pronounced for quadratic dust generation, as the large density variations obscure the temperature-dependent effects of the gas.

All the models produce a two-armed spiral. The arms are less pronounced for quadratic dust generation than for the linear dust generation because the former emphasizes regions of large planetesimal density. The density and extent of the arm diametrically opposite the companions can be reduced (and made more compatible with the observations) by diminishing the size of the initial disk (Fig. 16). The appearance of this arm can also be changed with a different encounter geometry. Larwood & Kalas (2001) show that, in an encounter between a circumstellar disk and a passing star, the spiral arm opposite the projectile is affected by the indirect tidal component of the potential, which diminishes as the collision becomes more hyperbolic.

In general, the models with quadratic dust generation produce more disorganized images than the models with linear dust generation. Planetesimal condensates are strong sources of dust that produce noise in the models. However, they also produce more peaked surface density profiles, which match the observed profiles better. Flatter initial density profiles (not shown here) produce large amounts of dust at large distances. Disks with initial radii larger than $\sim$1000 AU produce remnant structures that are not observed, including very long spiral arms. Conversely, disks with an initial radius of 400 AU yield dust distributions that reproduce well the observed large-scale arms and surface density profiles (Fig. 16). We surmise from our models that HD 141569A's initial planetesimal and gas disks had radii $\lesssim$700 AU and 10–50 $M_\oplus$ of $H/r = 0.1$ gas (Fig. 17).

4.3. *The Effect of Giant Planets*

From Figure 11 it seems clear that different dust configurations (i.e., large holes) can be created by manipulating the dust generation history of the system. The size of the hole can

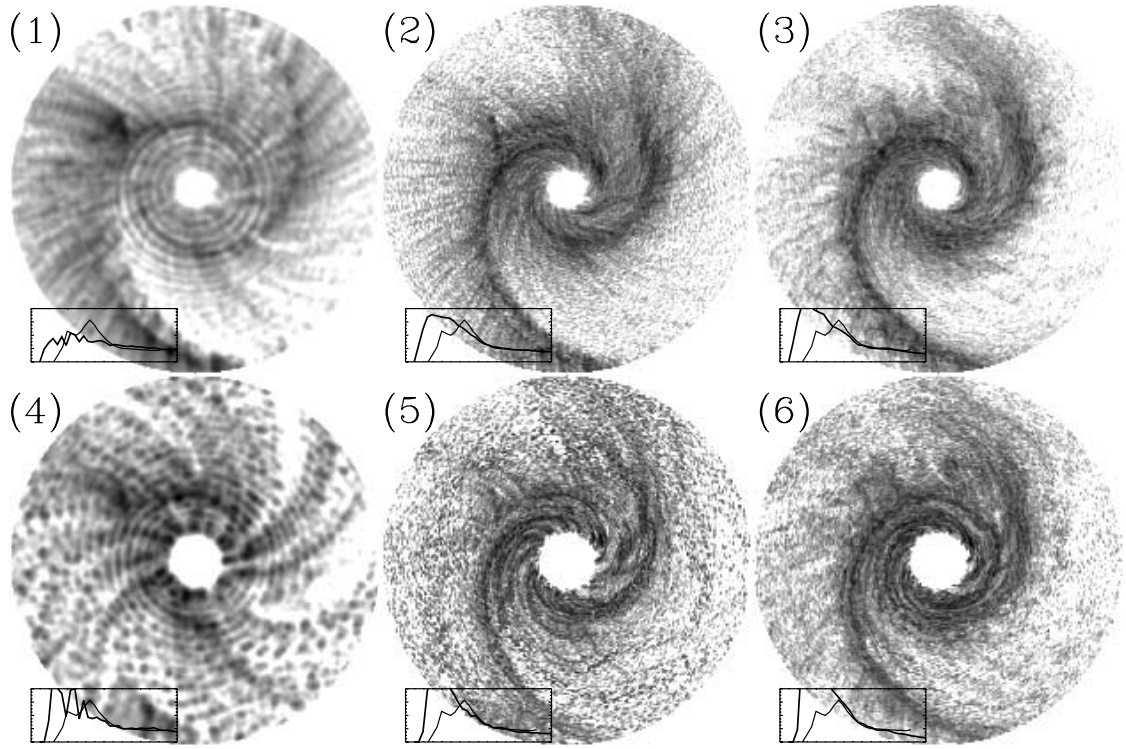

FIG. 14.—Same as Fig. 13, but with $\beta = 10$. The concentric rings for the gasless models are artifacts from the dust generation process.

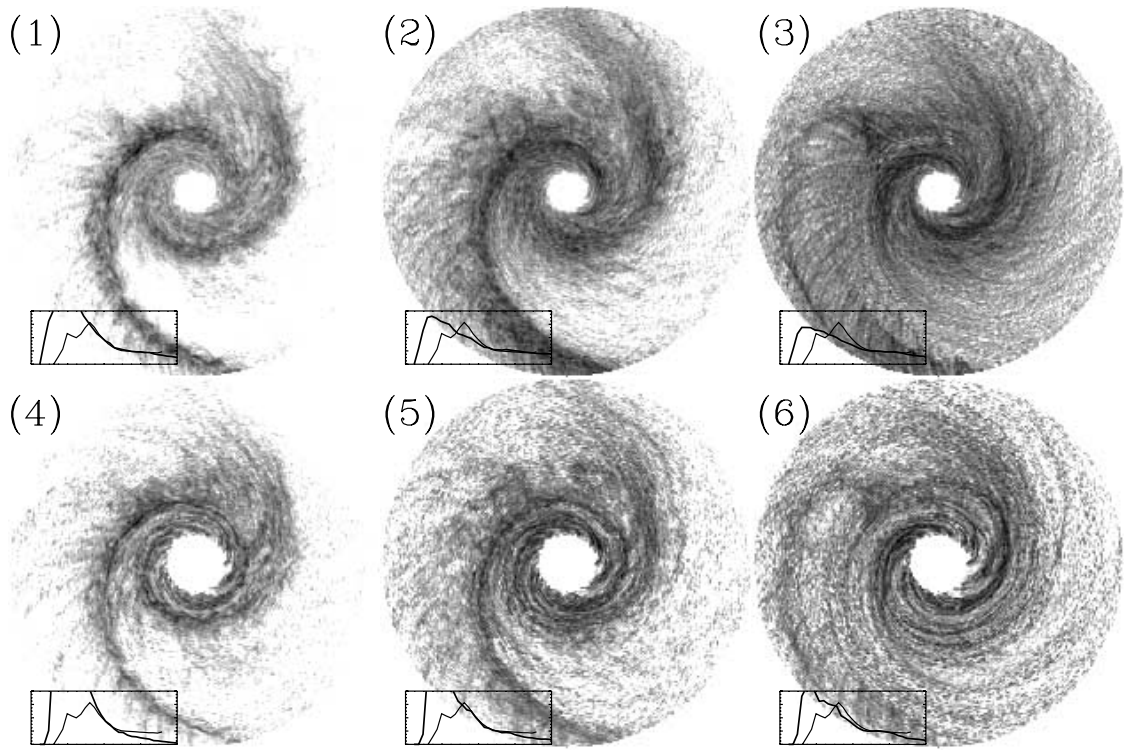

FIG. 15.—Effect of the gas temperature on the dust distribution. All models have $\beta = 4$ and 50 $M_{\oplus}$ of gas. *Top*, Results of the linear dust generation method; *bottom*, results of the quadratic one. *Top, left to right*: (1) Gas with $H/r = 0.05$, linear dust generation; (2) gas with $H/r = 0.1$, linear dust generation; (3) LTE, linear dust generation. *Bottom, left to right*: (4) gas with $H/r = 0.05$, quadratic dust generation; (5) gas with $H/r = 0.1$, quadratic dust generation; (6) LTE, quadratic dust generation.

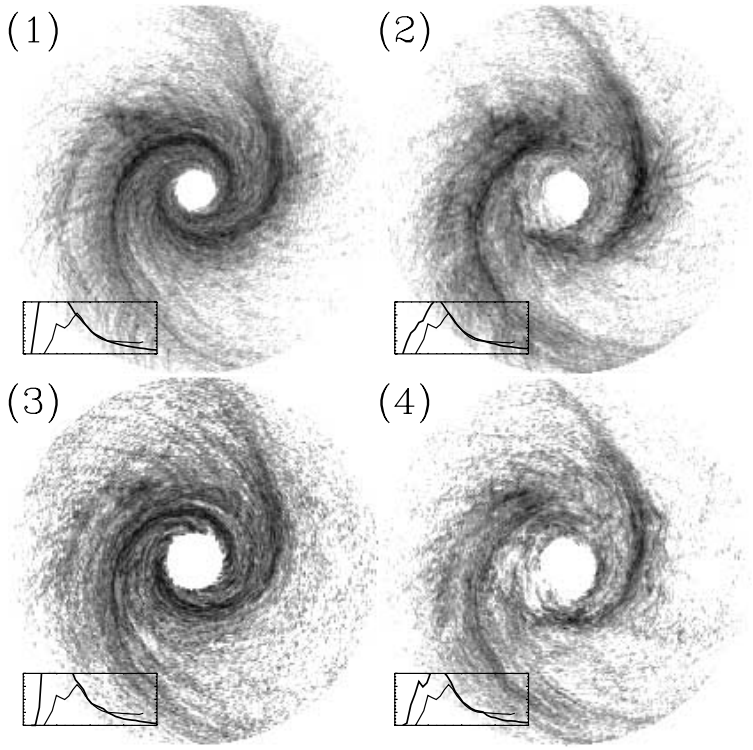

FIG. 16.—Planets and small disks. *Top*, linear dust generation; *bottom*, quadratic dust generation. All simulations have $\beta = 4$, with 50 $M_\oplus$ of $H/r = 0.1$ gas. (1) 400 AU initial disk, linear dust generation; (2) 400 AU initial disk, linear dust generation, with an eccentric ($e = 0.6$), $5M_J$ planet with semimajor axis 100 AU; (3) 400 AU initial disk, quadratic dust generation; (4) 400 AU initial disk, quadratic dust generation, with an eccentric $5M_J$ planet within 160 AU.

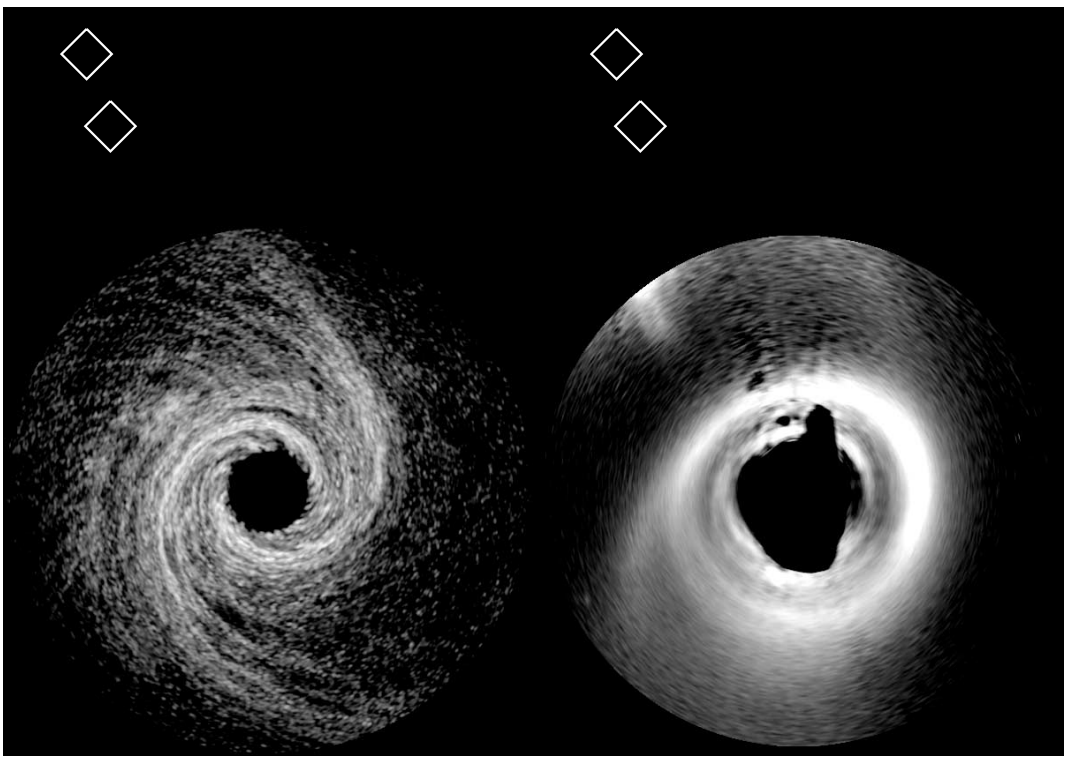

FIG. 17.—Comparison between best model and observations. Both are logarithmic stretches. The model ($\beta = 4$, with 50 $M_\oplus$ of $H/r = 0.1$ gas, quadratic dust generation, with an eccentric $5M_J$ planet within 100 AU) has been rotated counterclockwise by 13°.

be controlled by varying β or the time between dust generations. Although theoretically possible, such contrived scenarios are physically unreasonable.

A more reasonable agent for creating a hole in the dust distribution is a planet (or planets) within ~150 AU. If large enough, planets would clear out the planetesimals and the gas and create a region without dust. Each planet would sweep up a lane along its orbit as wide as a few times its Hill radius, R_H. From Bryden et al. 2000, a $5M_J$ planet with a semimajor axis of 100 AU and eccentricity $e = 0.6$ would clear a region with a half-width of 90 AU. Alternatively, multiple planets in less eccentric orbits would have a similar effect.

Here we present exploratory simulations that include the effect of a giant planet. Panels 2 and 4 of Figure 16 show models that include a $5M_J$ planet in an eccentric orbit ($e \sim 0.6$) around HD 141569A with a semimajor axis of 100 AU. The planet clears the central region enough to greatly reduce the dust generation close to the star and produce an inner hole in the dust disk. Weak signatures of the eccentricity (the elongated shape and slight dust overdensities at the top and the bottom of the hole) are observed. The inner ring in the observed density profile is not reproduced in the observations, at least with these orbital parameters. Considering the uncertainties in the exact dust configuration close to the coronagraphic mask, this is a satisfactory result. A $5M_J$ planet of age 5 Myr would be $\sim 10^{-5}$ times less luminous, and over 12 mag fainter in K than HD 141569A (Burrows et al. 1997; Golimowski et al. 2004). Such an planet would be below the noncoronagraphic NICMOS detection limits (Krist et al. 1998).

The formation of small planets may produce sharp rings in the disk by stirring nearby planetesimals and enhancing dust generation. This process has been modeled in detail by Kenyon & Bromley (2004). Both this effect and the presence of a giant planet modeled above produce inner ring variability on timescales of ~1000 yr.

5. DISCUSSION

Our favored model of the scattered-light disk is shown in Figure 17. This model assumes an initial disk size of 400 AU, $\beta = 4$, and gas with mass 50 $M_\oplus$ and an opening angle of $H/r = 0.1$. The model reproduces the large-scale spiral arms and, despite a large value of β, produces localized structures. It does not reproduce the sharp and coherent rings or disk asymmetries of the disk around HD 141569A, as observed by C03, which suggests that a different encounter geometry should be considered. The model includes a $5M_J$ planet in an eccentric orbit ($e = 0.6$) with apastron 160 AU for the purpose of clearing out a region of planetesimals close to the central star. The characteristics of this planet are not tightly constrained by the model, and other configurations (including multiple planets) are possible. The simulations clearly indicate that a mechanism capable of clearing the inside of the disk (like a planet or planets) is necessary to explain the observed density profile. There may be additional observational evidence supporting the existence of a planet. Brittain & Rettig (2002) have detected H_3^+ within 7 AU of HD 141569A, which they suggest may come from the extended atmosphere from a giant protoplanet.

Although there is favorable evidence for the existence of a planet or planets, we should also consider the effect of ice condensation on the surface density of the dust. An abrupt change in the surface density is expected upon crossing the "snow line," which for HD 141569A's disk is ~150 AU (LL03). The location of the snow line depends strongly on grain size, so it likely varies with observed wavelength. Current coronagraphic images lack the spectral resolution needed to probe these variations. While crossing the snow line cannot explain the paucity of dust close to the star, it likely affects the shape of the observed surface density.

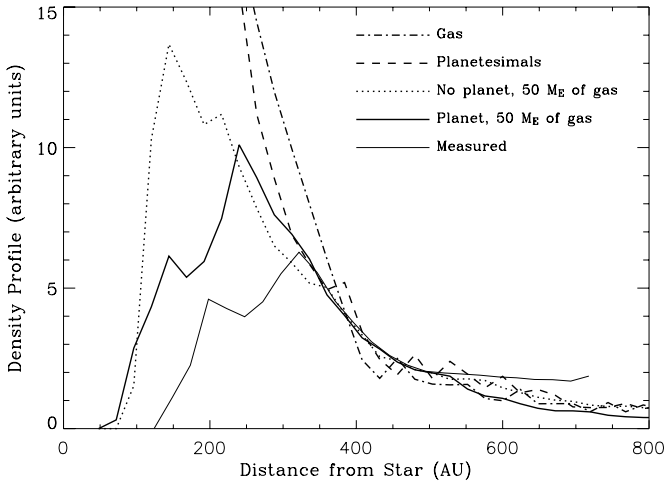

FIG. 18.—Comparison between measured and modeled profiles at $T = 1.50$. The traces show density profiles generated quadratically in small disks ($\beta = 4$, with 50 $M_\oplus$ of $H/r = 0.1$ gas), with and without planets (Fig. 16, panels 3 and 4). Also shown are the planetesimal and gas surface densities. These are steeper than those initially set because of the truncating effect of the encounter.

Most of the gas simulations do a similar job of reproducing the optical depth images and profiles. It would seem that the only hard constraint that they provide is that the presence of gas is necessary. The quadratic dust generation method does a somewhat better job than the linear one in matching the density profiles. Interestingly, Figure 18 shows that the planetesimal distribution itself can also match the outer surface density profile. The surface density of planetesimals starts as $r^{-1.5}$, but the truncation by the encounter makes it steeper by the time the simulations are examined. The surface density of dust generated quadratically also matches the distribution of planetesimals: while the dust is generated as the square of the planetesimal distribution, it is blown outward by radiation pressure. This process tends to flatten the simulated profile.

The applicability of our models to the debris disk around HD 141569A depends on the premise that the observed dust grains are small enough so that $\beta > 1$. This condition is borne out by the disk colors, the mean scattering phase, and thermal models. Could larger particles ($\beta < 0.5$) be contributing to the observed scattered light image? In deriving the scattering-opacity function (Fig. 2), we assumed that the collisional equilibrium timescale is smaller than any other systemic timescale, which implies that the number of grains of size s decreases as $s^{-3.5}$. If small grains were more quickly removed from their points of creation, then an excess of larger grains would result because they would no longer suffer erosion from collisions with the smaller grains (Thébault et al. 2003). In the absence of gas, $\beta < 0.5$ grains are eliminated by PR drag on timescales orders of magnitude larger than the RP timescales (Chen & Jura 2001), so the proportion of larger grains would further increase. However, in the presence of modest amounts of gas, $\beta < 0.5$ grains migrate to stationary orbits (TA01) and small particles settle down at the outer edge of the disk. The timescale over which this migration occurs is quite small for small grains but is larger than the purely dynamical timescales associated with $\beta > 0.5$ motions. All these processes may alter the shape of the dust size distribution. If, for example, the distribution is flatter than $s^{-3.5}$, then the peak of the

scattering-opacity function is broadened. While the optical image of the disk may still be dominated by β-meteoroids, the contributions of larger, bound grains may be significant.

The entangled roles of RP, gas drag, and the dynamical role of the companions greatly complicate any effort to model all components of the disk. To do so successfully requires multiwavelength images of the disk. Observations by the *Spitzer Space Telescope* should soon help this situation, as *Spitzer* will observe larger grains that are less affected by RP. Future observations with the Atacama Large Millimeter Array (ALMA) will also contribute valuable information about the composition and distribution of the dust.

6. CONCLUSIONS

We have developed dynamical models to investigate the structures observed in the debris disk around HD 141569A. The models include, for the first time, the effects of radiation pressure and gas drag. The disk's colors and scattering phase indicate that the scattered-light images are produced by submicron-sized dust grains. To understand these images, we must consider the behavior of grains with values of β (the ratio of radiation and gravitational forces) larger than 1. These grains are expelled from the disk in shorter than dynamical timescales. We show that up to 60 $M_\oplus$ of gas may be present in the disk. Gas drag slows the blowout of grains and is fundamental to understanding the structure of the disk.

If the dust is continuously created, its steady state surface density is featureless and has a radial profile dependent on the amount of gas and the prescription for dust creation. To produce a broad ring of dust, its creation must be prevented within some inner radial limit (Fig. 7). In principle, one can use the observed surface density profile to estimate the amount of mass lost by the disk throughout its history. However, because large grains remain in the disk longer than smaller grains, this estimation implies an implausible amount of solid material in the disk. Consequently, either the observed rate of dust generation is limited to times near the encounter of the disk with HD 141569A's binary companions, or small grains are created highly preferentially over larger ones.

Inspired by the disk's large-scale spiral arms, we explored the effect on the disk from a parabolic flyby of the binary companions. Such an encounter is consistent with the measured proper motion of the system. Our models consider the dynamical evolution of three different populations: planetesimals (subject only to gravity), gas (subject to gravity and hydrodynamic forces), and dust (subject to gravity, radiation pressure, and gas drag). The Poynting-Robertson effect, self-gravity, and the dynamical effects of collisions are ignored. We vary β, the initial gas mass, the gas disk opening angle, and the prescription for dust generation. We find that the dust distribution resembles that of the contemporary planetesimal distribution. The models are most sensitive to the gas temperature, with hotter gas producing more disorganized structures than colder gas. Five-fold differences in the gas mass and two-fold differences in β do not produce significant differences in the simulated disks. Quadratic dust generation produces more disorganized and less distinct structures than linear dust generation. Smaller initial disks produce smaller and less pronounced spiral arms.

Our favored model (Fig. 17) has an initial disk size of 400 AU, $\beta = 4$, and gas with mass 50 $M_\oplus$ and an opening angle of $H/r = 0.1$. A planet is introduced to reduce the surface density of the planetesimals close to the central star, but the characteristics of this planet are not tightly constrained. The model successfully reproduces the large-scale structures seen in the scattered-light images of the disk. However, the model does not reproduce the tightly wound spiral rings or other observed asymmetries, which suggests that another population of grains (perhaps with smaller β) or a noncoplanar encounter geometry should be investigated.

The authors thank B. Zuckerman, T. Forveille, and J. Kastner for generously providing the data from their 1995 paper. We are grateful to K. Anderson, W. J. McCann, S. Busching, A. Framarini, and T. Allen for their invaluable contributions to the ACS project at JHU. ACS was developed under NASA contract NAS5-32865, and this research has been supported by NASA grant NAG5-7697. We are grateful for an equipment grant from Sun Microsystems, Inc. The Space Telescope Science Institute is operated by the Association of Universities for Research in Astronomy (AURA), Inc., under NASA contract NAS5-26555. Furthermore, we gratefully acknowledge support from NASA Origins of Solar Systems grants NAG5-10732 and NNG04GG50G. Finally, we wish to thank the anonymous referee whose comments greatly improved the paper.

REFERENCES

Augereau, J. C., Lagrange, A. M., Mouillet, D., & Ménard, F. 1999, A&A, 350, L51
Augereau, J. C., & Papaloizou, J. C. B. 2004, A&A, 414, 1153
Backman, D. E., & Paresce, F. 1993, in Protostars and Planets III, ed. E. H. Levy & J. I. Lunine (Tucson: Univ. Arizona Press), 1253
Beckwith, S. V. W., & Sargent, A. I. 1993, ApJ, 402, 280
Bohren, C. F., & Huffman, D. R. 1983, Absorption and Scattering of Light by Small Particles (New York: Wiley)
Brandeker, A., Liseau, R., Olofsson, G., & Fridlund, M. 2004, A&A, 413, 681
Brittain, S. D., & Rettig, T. W. 2002, Nature, 418, 57
Bryden, G., Lin, D. N. C., & Ida, S. 2000, ApJ, 544, 481
Burrows, A., et al. 1997, ApJ, 491, 856
Chen, C. H., & Jura, M. 2001, ApJ, 560, L171
Clampin, M., et al. 2003, AJ, 126, 385 (C03)
Draine, B. T., & Lee, H. M. 1984, ApJ, 285, 89
Fisher, R. S., Telesco, C. M., Piña, R. K., Knacke, R. F., & Wyatt, M. C. 2000, ApJ, 532, L141
Golimowski, D. A., et al. 2004, AJ, 127, 3516
Kenyon, S. J., & Bromley, B. C. 2004, AJ, 127, 513
Krist, J. E., Golimowski, D. A., Schroeder, D. J., & Henry, T. J. 1998, PASP, 110, 1046
Lacy, J. H., Knacke, R., Geballe, T. R., & Tokunaga, A. T. 1994, ApJ, 428, L69
Laor, A., & Draine, B. T. 1993, ApJ, 402, 441
Larwood, J. D., & Kalas, P. G. 2001, MNRAS, 323, 402
Lecavelier Des Etangs, A., Vidal-Madjar, A., & Ferlet, R. 1996, A&A, 307, 542
———. 1998, A&A, 339, 477
Li, A., & Lunine, J. I. 2003, ApJ, 594, 987 (LL03)
Marsh, K. A., Silverstone, M. D., Becklin, E. E., Koerner, D. W., Werner, M. W., Weinberger, A. J., & Ressler, M. E. 2002, ApJ, 573, 425
Miyake, K., & Nakagawa, Y. 1993, Icarus, 106, 20
Monaghan, J. J. 1992, ARA&A, 30, 543
Mouillet, D., Lagrange, A. M., Augereau, J. C., & Ménard, F. 2001, A&A, 372, L61
Osterloh, M., & Beckwith, S. V. W. 1995, ApJ, 439, 288
Ozernoy, L. M., Gorkavyi, N. N., Mather, J. C., & Taidakova, T. A. 2000, ApJ, 537, L147
Quillen, A. C., Varniere, P., Minchev, I., & Frank, A. 2005, AJ, 129, 2481
Sylvester, R. J., Dunkin, S. K., & Barlow, M. J. 2001, MNRAS, 327, 133
Takeuchi, T., & Artymowicz, P. 2001, ApJ, 557, 990 (TA01)
Thébault, P., Augereau, J. C., & Beust, H. 2003, A&A, 408, 775
Weinberger, A. J., Becklin, E. E., Schneider, G., Smith, B. A., Lowrance, P. J., Silverstone, M. D., Zuckerman, B., & Terrile, R. J. 1999, ApJ, 525, L53
Weinberger, A. J., Rich, R. M., Becklin, E. E., Zuckerman, B., & Matthews, K. 2000, ApJ, 544, 937
Wood, K., Smith, D., Whitney, B., Stassun, K., Kenyon, S. J., Wolff, M. J., & Bjorkman, K. S. 2001, ApJ, 561, 299
Zuckerman, B. 2001, ARA&A, 39, 549
Zuckerman, B., Forveille, T., & Kastner, J. H. 1995, Nature, 373, 494